

## On the Cross-Polarization Levels of Arrays With Wide Angle Impedance Matching Layers

Van Katwijk, Alexander J.; Coco Martin, C.M.; Toso, Giovanni; Cavallo, Daniele

**DOI**

[10.1109/TAP.2024.3394208](https://doi.org/10.1109/TAP.2024.3394208)

**Publication date**

2024

**Document Version**

Final published version

**Published in**

IEEE Transactions on Antennas and Propagation

**Citation (APA)**

Van Katwijk, A. J., Coco Martin, C. M., Toso, G., & Cavallo, D. (2024). On the Cross-Polarization Levels of Arrays With Wide Angle Impedance Matching Layers. *IEEE Transactions on Antennas and Propagation*, 72(6), 5078-5087. <https://doi.org/10.1109/TAP.2024.3394208>

**Important note**

To cite this publication, please use the final published version (if applicable). Please check the document version above.

**Copyright**

Other than for strictly personal use, it is not permitted to download, forward or distribute the text or part of it, without the consent of the author(s) and/or copyright holder(s), unless the work is under an open content license such as Creative Commons.

**Takedown policy**

Please contact us and provide details if you believe this document breaches copyrights. We will remove access to the work immediately and investigate your claim.

***Green Open Access added to TU Delft Institutional Repository***

***'You share, we take care!' - Taverne project***

**<https://www.openaccess.nl/en/you-share-we-take-care>**

Otherwise as indicated in the copyright section: the publisher is the copyright holder of this work and the author uses the Dutch legislation to make this work public.

# On the Cross-Polarization Levels of Arrays With Wide Angle Impedance Matching Layers

Alexander J. van Katwijk<sup>1</sup>, *Member, IEEE*, Caspar M. Coco Martin<sup>2</sup>, *Graduate Student Member, IEEE*, Giovanni Toso<sup>3</sup>, *Fellow, IEEE*, and Daniele Cavallo<sup>4</sup>, *Senior Member, IEEE*

**Abstract**—The characteristic cross-polarization (X-pol) of wide angle impedance matching (WAIM) structures is investigated. The study considers an ideal linearly polarized current sheet in the presence of various dielectric and artificial dielectric superstrates, analyzed using transmission line models representing the stratified media. The main mechanism that causes increased X-pol is highlighted and linked to the anisotropy of the superstrate. We then propose an approach to reduce the X-pol by including vertical vias within the WAIM dielectrics, to control the vertical component of the permittivity tensor. The intrinsic X-pol performance of a set of artificial dielectric layers (ADLs) with and without vias is experimentally verified by placing the WAIM above an open-ended waveguide that acts as a linearly polarized source. The proposed WAIM with vias can be used in wideband wide-scanning array designs to improve polarization purity.

**Index Terms**—Artificial dielectric layers (ADLs), cross-polarization (X-pol), Wheeler’s current, wide angle impedance matching (WAIM).

## I. INTRODUCTION

WIDEBAND wide-scanning antenna arrays gained popularity in the last decade because of their capability to support multiple functions within a single radiating aperture. For some applications, such as radio astronomy and satellite communications, polarization purity becomes an important requirement. However, most of the existing wideband arrays trade-off efficiency and polarization purity for bandwidth and scan range.

Planar array designs often utilize dielectric slabs or metal structures placed above the antenna (superstrates) to improve the matching performance and the scanning capability [1], [2]. One such superstrate is the wide angle impedance matching (WAIM) layer [3], which consists of an electrically

thin dielectric layer located in the close vicinity of the array to mitigate the impedance mismatch while scanning. Since its introduction, various research efforts have gone into exploiting metasurfaces in WAIM designs to improve the array performance in terms of scanning range or operational bandwidth [4], [5].

Another approach to realizing superstrates was presented in [6], [7], and [8] and proposes using artificial dielectric layers (ADLs) rather than homogeneous isotropic dielectrics. ADLs consist of periodic metallic patches, small with respect to the wavelength, embedded in a host material to create an equivalent material with modified properties. The effective electromagnetic parameters of the artificial material can be engineered by properly designing the spatial density of the metallic inclusions. ADLs are anisotropic, which is a key advantage that helps avoid the occurrence of surface waves and scan blindness, even for very large scanning angles.

Although dielectric and metal WAIMs have been extensively studied with a focus on the matching and scan performance, they have not been thoroughly investigated in terms of polarization properties. On the other hand, it is known that dielectric slabs can influence the polarization performance of antennas, e.g., dielectric substrates increase the cross-polarization (X-pol) levels of microstrip antennas, especially in the diagonal planes [9]; also, dielectric superstrates increase the axial ratio in circularly polarized arrays [10].

In this article, we first describe the fundamental limits of dielectric and artificial dielectric superstrates in terms of X-pol. To highlight the main mechanism, an ideal Wheeler current sheet [11] is considered in the presence of different superstrates. The X-pol behavior is then studied using transmission line models representing stratified media. Based on this study, we identify the effective anisotropy of WAIMs as the main cause of X-pol deterioration. We then propose an approach to reduce the X-pol levels while maintaining comparable bandwidth performance. To do so, we add vias in some parts of the dielectrics to enhance the vertical component of the effective permittivity tensor. To validate the proposed concept, an ADL superstrate with and without vias is manufactured and tested, showing reduced X-pol when vias are included.

## II. CROSS-POLARIZATION OF WHEELER’S CURRENT SHEET WITH A SUPERSTATE

To better understand the intrinsic polarization properties of common superstrates, it is convenient to first introduce the

Manuscript received 13 February 2024; revised 10 April 2024; accepted 22 April 2024. Date of publication 2 May 2024; date of current version 7 June 2024. This work was supported in part by European Space Agency (ESA) through the Project “Antenna User Terminal With Wide Angle Impedance Matching Metamaterial Radome” under Contract 4000127381/19/NL/AF. (Corresponding author: Alexander J. van Katwijk.)

Alexander J. van Katwijk, Caspar M. Coco Martin, and Daniele Cavallo are with the Microelectronics Department, EEMCS Faculty, Delft University of Technology, 2628 CD Delft, The Netherlands (e-mail: a.j.vankatwijk@tudelft.nl; c.m.cocomartin@tudelft.nl; d.cavallo@tudelft.nl).

Giovanni Toso is with the Radio Frequency Payloads and Technology Division, European Space Research and Technology Centre (ESTEC), European Space Agency (ESA), 2200 AG Noordwijk, The Netherlands (e-mail: giovanni.toso@esa.int).

Color versions of one or more figures in this article are available at <https://doi.org/10.1109/TAP.2024.3394208>.

Digital Object Identifier 10.1109/TAP.2024.3394208

polarization characteristics of an ideal source. To this aim, we consider a Wheeler's current sheet [11], which represents a current distribution with constant amplitude over an infinite plane and with a continuous linear phase distribution. For example, we can consider an  $x$ -oriented magnetic current sheet with constant amplitude  $V_0$  in the  $xy$  plane, infinitesimally thin in  $z$ , and with a phase distribution to point its radiated field to the angle  $\theta$  and  $\phi$

$$\mathbf{m}(x, y, z) = m_x(x, y, z)\hat{\mathbf{x}} = V_0 e^{-jk_{x0}x} e^{-jk_{y0}y} \delta(z)\hat{\mathbf{x}} \quad (1)$$

where  $k_{x0} = k_0 \sin \theta \cos \phi$  and  $k_{y0} = k_0 \sin \theta \sin \phi$ ,  $k_0$  is the free-space wavenumber and  $\delta(\cdot)$  is the Dirac delta function. The Wheeler current is equivalent to a phased array with infinitesimally small spacing, yielding a continuous phase distribution rather than the discrete one.

Generally, the radiated X-pol from a current sheet depends on the stratification above and below. However, for the sake of simplicity, we assume that the magnetic current is located on a perfect electric conductor (PEC) sheet so that only the stratification above the radiating plane is considered. This assumption is relevant in the context of slot arrays because the metallic plate in which the slots are etched typically decouples the radiation in the half spaces above and below the slots.

To find the field radiated by the Wheeler current sheet in the presence of a dielectric or metal stratification, such as the one shown in Fig. 1(a), one can make use of the spectral Green's function for stratified media  $\bar{\mathbf{G}}^{em}$  [12] that relates the electric field to a magnetic source. The  $x$ -,  $y$ -, and  $z$ -components of the electric field can be calculated as described in Appendix A and are given by

$$\begin{aligned} e_x &= V_0 G_{xx}^{em}(k_{x0}, k_{y0}) = V_0 (v_{TM} - v_{TE}) \sin \phi \cos \phi \\ e_y &= V_0 G_{yx}^{em}(k_{x0}, k_{y0}) = V_0 (v_{TE} \cos^2 \phi + v_{TM} \sin^2 \phi) \\ e_z &= V_0 G_{zx}^{em}(k_{x0}, k_{y0}) = -V_0 \zeta_0 i_{TM} \sin \theta \sin \phi \end{aligned} \quad (2)$$

where  $G_{xx}^{em}$ ,  $G_{yx}^{em}$ , and  $G_{zx}^{em}$  are the relevant components of the dyadic Green's function for an  $x$ -oriented magnetic current. These components can be expressed in terms of the current and voltage solutions ( $i_{TE}$ ,  $i_{TM}$ ,  $v_{TE}$ , and  $v_{TM}$ ) of the equivalent transmission lines representing the stratification, as depicted in Fig. 1(b). Two transmission lines are considered for the transverse electric (TE) and transverse magnetic (TM) modes, with characteristic impedances  $Z_{TE} = \zeta_0 k_0 / k_z$  and  $Z_{TM} = \zeta_0 k_z / (k_0 \epsilon_r)$ , respectively, where  $\zeta_0 = 120\pi \Omega$  is the free-space medium impedance,  $k_z = (\epsilon_r k_0^2 - k_{x0}^2 - k_{y0}^2)^{0.5}$  is the propagation constant in the transmission line section, and  $\epsilon_r$  is the relative permittivity of the dielectric layer. The currents and voltages can be calculated at any point  $z > z_0$  above the stratification, assuming a normalized voltage generator of 1 V. It should be noted that in (2), we omit the phase term  $\exp(-jk_0 r)$  that multiplies all the components, with  $r$  being the distance from the observation point to the point  $(x, y, z) = (0, 0, z_0)$ .

The Cartesian components of the field can be projected onto the co- and cross-polarized vectors, defined according to the third definition of Ludwig [13]. Following the steps reported

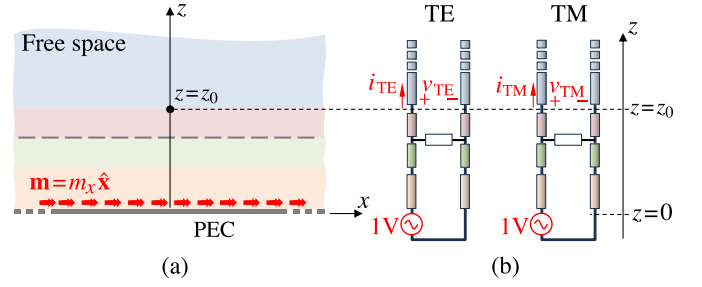


Fig. 1. (a) Wheeler current sheet on a PEC plane loaded with a generic dielectric/metal stratification. (b) Equivalent transmission lines for TE and TM modes.

in Appendix B, the X-pol ratio can be written as follows:

$$X_{\text{pol}}(\theta, \phi) = \frac{e_{\text{cr}}}{e_{\text{co}}} = \frac{\frac{\sin(2\phi)}{2} (v_{TM} \sec \theta - v_{TE})}{v_{TM} \sin^2 \phi \sec \theta + v_{TE} \cos^2 \phi}. \quad (3)$$

It is evident from (3) that for scanning in the main planes ( $\phi = 0^\circ$  or  $\phi = 90^\circ$ ) the X-pol is always 0 for any planar stratification. Another specific case is the diagonal plane ( $\phi = 45^\circ$ ), typically associated with the highest X-pol levels, for which the expression of the X-pol becomes

$$X_{\text{pol}}(\theta, \phi = 45^\circ) = \frac{v_{TM} \sec \theta - v_{TE}}{v_{TM} \sec \theta + v_{TE}}. \quad (4)$$

#### A. Free-Space Case

In the case of a Wheeler's current sheet radiating in free space [Fig. 2(a)], the voltages  $v_{TE}$  and  $v_{TM}$  are equal to 1, yielding a simple expression for the X-pol

$$X_{\text{pol}}(\theta, \phi) = \frac{\frac{\sin(2\phi)}{2} (\sec \theta - 1)}{\sin^2 \phi \sec \theta + \cos^2 \phi}. \quad (5)$$

For the diagonal plane, this simplifies to

$$X_{\text{pol}}(\theta, \phi = 45^\circ) = \frac{\sec \theta - 1}{\sec \theta + 1} = \tan^2 \frac{\theta}{2}. \quad (6)$$

In free space,  $v_{TE}$  and  $v_{TM}$  are constant with frequency, so the X-pol is also frequency independent. In Fig. 2(b), the X-pol is plotted as a function of the scan angle  $\theta$ , for  $\phi = 45^\circ$ . It is visible that, even for a perfectly linear polarized array radiating in free space, the X-pol increases with  $\theta$  and reaches about  $-9.5$  dB for  $\theta = 60^\circ$  in the diagonal plane. This value represents a benchmark to assess the performance of a wide-scanning array. The curve in Fig. 2(c) shows the X-pol for  $\theta = 60^\circ$  and varying  $\phi$ . As expected, the maximum X-pol occurs around the diagonal planes.

#### B. Dielectric Superstrate

When adding a homogeneous dielectric slab above the current, the radiated fields vary with frequency and depend on the permittivity and thickness of the superstrate. A schematic of the structure and the corresponding equivalent circuit is given in Fig. 3(a). To calculate the voltages  $v_{TE}$  and  $v_{TM}$ , we can define the ABCD matrix of the slab as follows:

$$\begin{bmatrix} A & B \\ C & D \end{bmatrix}_{\text{slab}} = \begin{bmatrix} \cos(k_z h) & j Z_{Ti} \sin(k_z h) \\ j Y_{Ti} \sin(k_z h) & \cos(k_z h) \end{bmatrix} \quad (7)$$

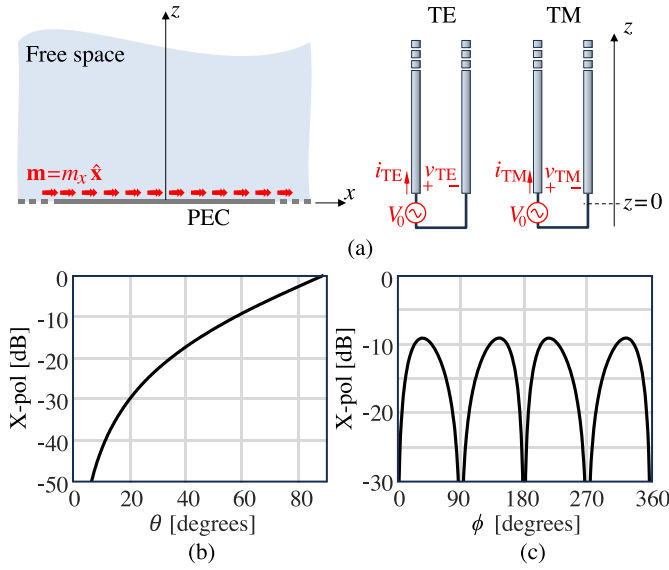


Fig. 2. (a) Wheeler magnetic current sheet radiating in free space and equivalent transmission lines for TE and TM modes. (b) X-pol for fixed  $\phi = 45^\circ$  and varying  $\theta$  and (c) for fixed  $\theta = 60^\circ$  and varying  $\phi$ .

where “ $T_i$ ” can indicate TE or TM and  $Y_{T_i} = 1/Z_{T_i}$ . The voltage and current at  $z = 0$  are

$$v_{T_i}(z = 0) = 1, \quad i_{T_i}(z = 0) = 1/Z_{in,T_i} \quad (8)$$

with

$$Z_{in,T_i} = Z_{T_i} \frac{Z_{0T_i} + jZ_{T_i} \tan(k_z h)}{Z_{T_i} + jZ_{0T_i} \tan(k_z h)}. \quad (9)$$

Here,  $Z_{0T_i}$  is the characteristic impedance for the free space transmission line. The voltage and current above the slab are found as follows:

$$\begin{bmatrix} v_{T_i}(z = z_0) \\ i_{T_i}(z = z_0) \end{bmatrix} = \begin{bmatrix} A & B \\ C & D \end{bmatrix}_{slab}^{-1} \begin{bmatrix} v_{T_i}(z = 0) \\ i_{T_i}(z = 0) \end{bmatrix}. \quad (10)$$

With some algebraic steps, we obtain

$$v_{T_i}(z = z_0) = \frac{V_0 Z_{0T_i}}{Z_{0T_i} \cos(k_z h) + jZ_{T_i} \sin(k_z h)}. \quad (11)$$

The X-pol at  $\phi = 45^\circ$  and  $\theta = 60^\circ$  for superstrates with  $h = \lambda_d/4$  and various relative permittivities is shown in Fig. 3(b). In these examples,  $\lambda_d$  is the wavelength in the dielectric at the frequency  $f_0$ . The free-space case ( $\epsilon_r = 1$ ) is also shown for comparison, corresponding to the constant curve. It can be observed that the X-pol of the dielectric slabs is always lower than the one of free space, with the case of  $\epsilon_r = 2$  being the one that gives the lowest values. Therefore, low permittivity superstrates could be used to reduce the X-pol of the array in specific frequency ranges. However, in realistic array designs with periodic elements, including such slabs would limit the scan range by supporting surface waves and causing scan blindness.

### C. Wide Angle Impedance Matching Layer

Another interesting case is where an air gap between the array and the dielectric slabs is included to implement a WAIM

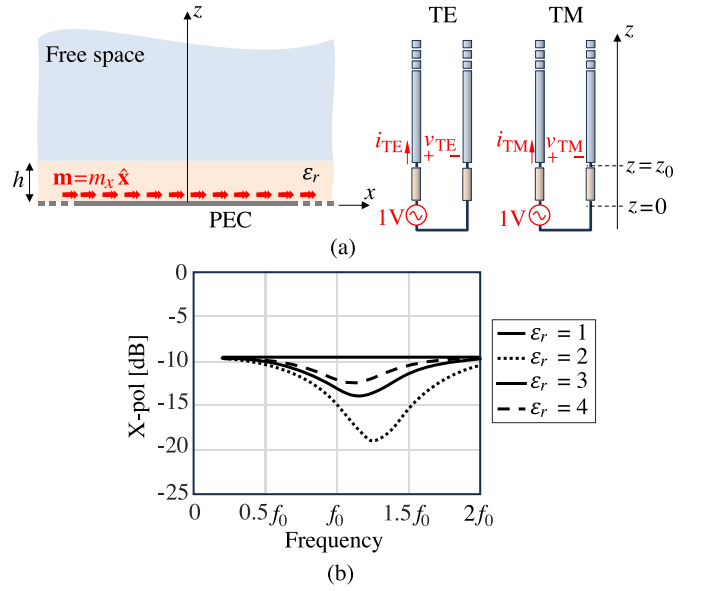


Fig. 3. (a) Wheeler current sheet radiating in the presence of a dielectric superstrate and equivalent transmission lines. (b) X-pol at  $\phi = 45^\circ$  and  $\theta = 60^\circ$ , for different values of permittivity.

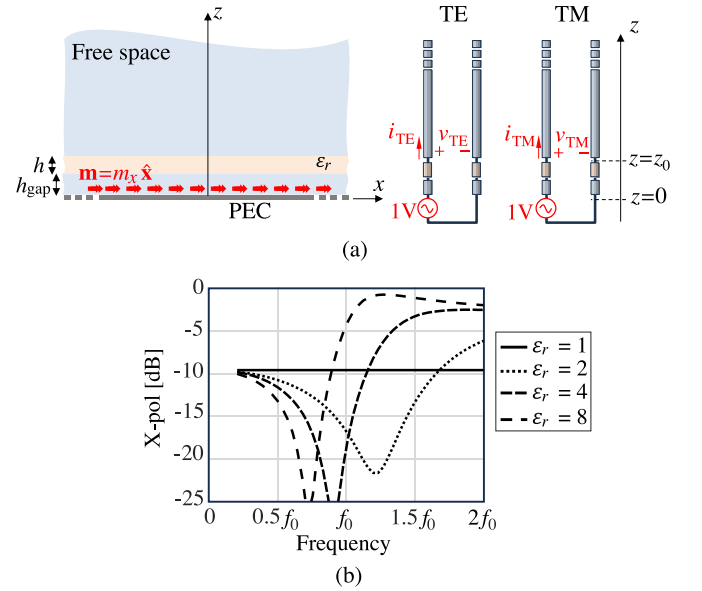


Fig. 4. (a) Wheeler current sheet radiating in the presence of a dielectric WAIM and equivalent transmission lines. (b) X-pol at  $\phi = 45^\circ$  and  $\theta = 60^\circ$ , for different values of permittivity.

layer [3]. This stratification is shown in Fig. 4(a). In this case,

$$\begin{bmatrix} A & B \\ C & D \end{bmatrix}_{strat} = \begin{bmatrix} A & B \\ C & D \end{bmatrix}_{gap} \begin{bmatrix} A & B \\ C & D \end{bmatrix}_{slab} \quad (12)$$

where the [ABCD] matrix of the slab is defined in (7) and

$$\begin{bmatrix} A & B \\ C & D \end{bmatrix}_{gap} = \begin{bmatrix} \cos(k_{z0} h_{gap}) & jZ_{0T_i} \sin(k_{z0} h_{gap}) \\ jY_{0T_i} \sin(k_{z0} h_{gap}) & \cos(k_{z0} h_{gap}) \end{bmatrix}. \quad (13)$$

The current at  $z = 0$  is given by  $i_{T_i}(z = 0) = 1/Z_{in,T_i}$ , where the input impedance is given by

$$Z_{in,T_i} = Z_{0T_i} \frac{Z'_{in,T_i} + jZ_{0T_i} \tan(k_{z0} h_{gap})}{Z_{0T_i} + jZ'_{in,T_i} \tan(k_{z0} h_{gap})} \quad (14)$$

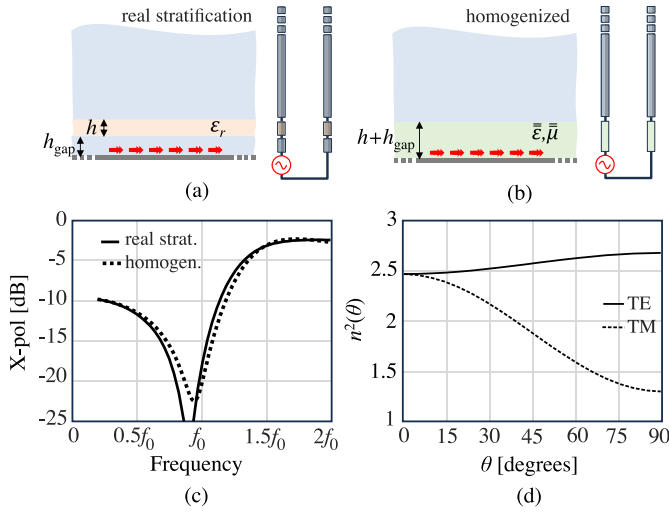


Fig. 5. (a) Real two-slab stratification with equivalent transmission line and (b) homogenized equivalent anisotropic slab. (c) X-pol at  $\phi = 45^\circ$  and  $\theta = 60^\circ$  for the two structures and (d) equivalent refractive index of the homogenized slab for TE and TM modes.

with

$$Z'_{\text{in},Ti} = Z_{Ti} \frac{Z_{0Ti} + jZ_{Ti} \tan(k_z h)}{Z_{Ti} + jZ_{0Ti} \tan(k_z h)}. \quad (15)$$

Fig. 4(b) shows the resulting X-pol at  $\phi = 45^\circ$  and  $\theta = 60^\circ$ , calculated for dielectric slabs with  $h = \lambda_d/10$  and  $h_{\text{gap}} = \lambda_0/10$ , where  $\lambda_0$  is the wavelength in free space. It can be observed that the X-pol exceeds the free-space values for the higher frequencies and can approach 0 dB for high permittivity. This observation is relevant because typical WAIM layers are characterized by high permittivity values [3].

The increase in X-pol can be explained by looking at the equivalent refractive index of the combination of the air gap and the dielectric. Using the method described in [14], the two slabs [Fig. 5(a)] can be replaced by a single homogenized slab [Fig. 5(b)] with equivalent permittivity and permeability tensors given by

$$\begin{bmatrix} \epsilon_x & 0 & 0 \\ 0 & \epsilon_y & 0 \\ 0 & 0 & \epsilon_z \end{bmatrix} = \begin{bmatrix} 2.6 & 0 & 0 \\ 0 & 2.6 & 0 \\ 0 & 0 & 1.2 \end{bmatrix} \quad (16)$$

$$\begin{bmatrix} \mu_x & 0 & 0 \\ 0 & \mu_y & 0 \\ 0 & 0 & \mu_z \end{bmatrix} = \begin{bmatrix} 0.95 & 0 & 0 \\ 0 & 0.95 & 0 \\ 0 & 0 & 1.2 \end{bmatrix}. \quad (17)$$

The X-pol radiated by the two structures is shown in Fig. 5(c) to be similar. One can write the refractive index for the TE and TM modes as follows [14]:

$$n_{\text{TE}} = \sqrt{\epsilon_y \mu_x + (1 - \mu_x/\mu_z) \sin^2 \theta} \quad (18)$$

$$n_{\text{TM}} = \sqrt{\epsilon_x \mu_y + (1 - \epsilon_x/\epsilon_z) \sin^2 \theta} \quad (19)$$

where  $\theta$  is the free-space propagation angle with respect to the axis of the material ( $z$ -axis). These indexes are shown as a function of the angle in Fig. 5(d). It is seen that the equivalent slab is characterized by an anisotropic behavior, where the TE and TM components of the field experience different refractive indexes at oblique incidence. Since the X-pol is given by the

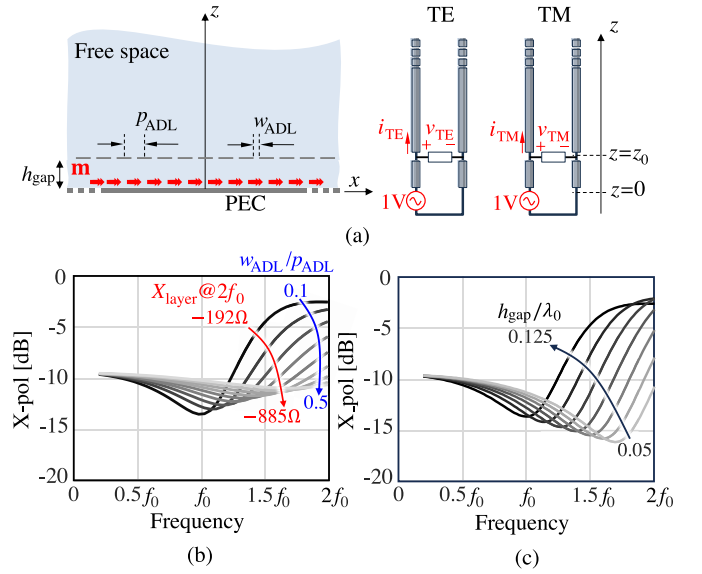


Fig. 6. (a) Wheeler current sheet radiating in the presence of a capacitive grid and equivalent transmission lines for TE and TM modes; X-pol at  $\phi = 45^\circ$  and  $\theta = 60^\circ$ , for different values of (b) gap width to period ratio  $w_{\text{ADL}}/p_{\text{ADL}}$ , which corresponds to varying layer reactance and (c) distance from the current.

ratio of the TE and TM voltages in the equivalent transmission line, the different refractive indexes cause an increase in X-pol.

#### D. Single Layer of Artificial Dielectric

A similar effect as the dielectric WAIM is observed when a capacitive grid is placed at a certain distance from the radiating current, as depicted in Fig. 6(a). The capacitive grid is an array of subwavelength square patches, which form a single layer of ADLs. The ABCD matrix of the stratification is given by

$$\begin{bmatrix} A & B \\ C & D \end{bmatrix}_{\text{strat}} = \begin{bmatrix} A & B \\ C & D \end{bmatrix}_{\text{gap}} \begin{bmatrix} A & B \\ C & D \end{bmatrix}_{\text{layer}} \quad (20)$$

where the ABCD matrix of the gap is defined in (13) and the ABCD matrix of the layer is given by

$$\begin{bmatrix} A & B \\ C & D \end{bmatrix}_{\text{layer}} = \begin{bmatrix} 1 & 0 \\ Y_{\text{layer},Ti} & 1 \end{bmatrix}. \quad (21)$$

The layer admittance is given by  $Y_{\text{layer},\text{TM}} = jB_{\text{layer}}$  and  $Y_{\text{layer},\text{TE}} = jB_{\text{layer}}(1 - 0.5\sin^2 \theta)$ , where  $B_{\text{layer}}$  is the equivalent susceptance of a layer, known in closed form [15], [16].

The current at  $z = 0$  is given by  $i_{Ti}(z = 0) = 1/Z_{\text{in},Ti}$ , with the input impedance equal to

$$Z_{\text{in},Ti} = Z_{0Ti} \frac{Z'_{\text{in},Ti} + jZ_{0Ti} \tan(k_{z0} h_{\text{gap}})}{Z_{0Ti} + jZ'_{\text{in},Ti} \tan(k_{z0} h_{\text{gap}})} \quad (22)$$

$$Z'_{\text{in},Ti} = \frac{1}{1/Z_{0Ti} + Y_{\text{layer},Ti}}. \quad (23)$$

The X-pol of a single metal layer with period  $p_{\text{ADL}} = \lambda_0/8$ , for  $\phi = 45^\circ$  and  $\theta = 60^\circ$ , is shown in Fig. 6. Similar to how the dielectric WAIM yields higher X-pol for higher permittivity, the X-pol of the metal layer increases for smaller layer reactance  $X_{\text{layer}} = -1/B_{\text{layer}}$ , which corresponds to narrower gaps  $w_{\text{ADL}}$  between patches. Fig. 6(b) shows the

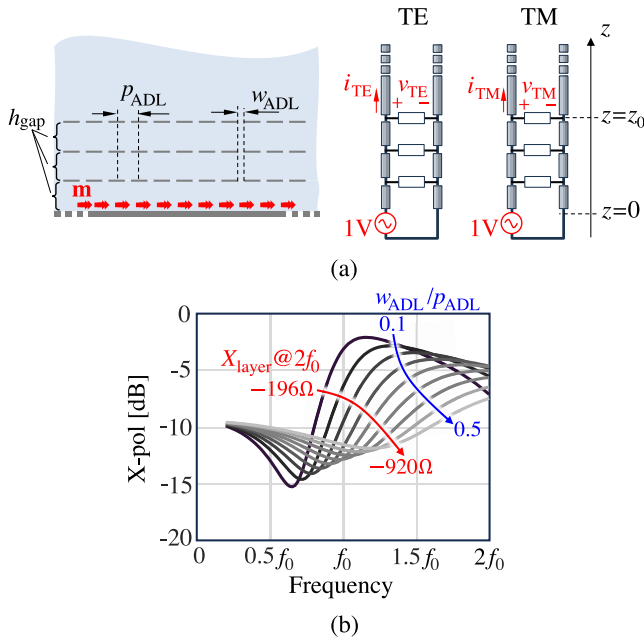


Fig. 7. (a) Wheeler current sheet radiating in the presence of a three-layer ADL structure and equivalent transmission lines for TE and TM modes. (b) X-pol at  $\phi = 45^\circ$  and  $\theta = 60^\circ$ , for varying gap width between the patches and corresponding layer reactance.

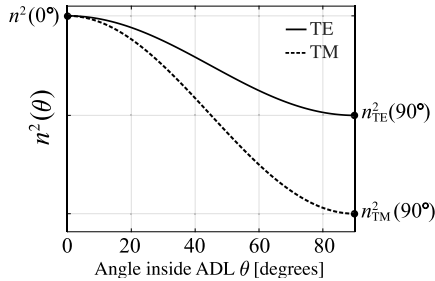


Fig. 8. Equivalent refractive index of a plane wave propagating through an ADL as a function of the angle inside the material.

X-pol for a layer placed at a distance  $h_{\text{gap}} = \lambda_0/8$  from the current sheet and different values of  $w_{\text{ADL}}$ . When fixing the gap width to  $w_{\text{ADL}} = 0.1p_{\text{ADL}}$  while varying the distance  $h_{\text{gap}}$ , the X-pol in Fig. 6(c) is obtained, which is shown to increase with the gap height.

When considering ADLs consisting of multiple metal layers, a similar effect occurs. The total ABCD matrix of the stratification can be found by cascading three times the air gap and the shunt layer capacitance in the equivalent transmission line. In Fig. 7 the X-pol for  $\phi = 45^\circ$  and  $\theta = 60^\circ$  of a three-layer ADL with period  $p_{\text{ADL}} = \lambda_0/8$ , interlayer distance  $h_{\text{gap}} = \lambda_0/16$ , and varying  $w_{\text{ADL}}$  is plotted. The X-pol increases for ADLs with higher metal density, which corresponds to higher effective permittivity.

### III. RELATIONSHIP BETWEEN X-POL AND ANISOTROPY

Similar to the WAIM, the higher X-pol in the presence of ADLs is caused by their anisotropy. The characteristic equivalent refractive index of ADLs is shown in Fig. 8. It is seen that an ADL slab has an equivalent refractive index that changes with the incidence angle and changes differently for the TE and TM modes. Similar to the dielectric WAIM

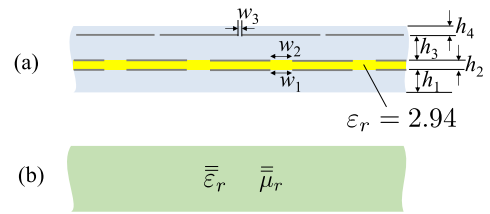


Fig. 9. (a) Considered ADL stratification and (b) equivalent anisotropic material resulting from the homogenization.

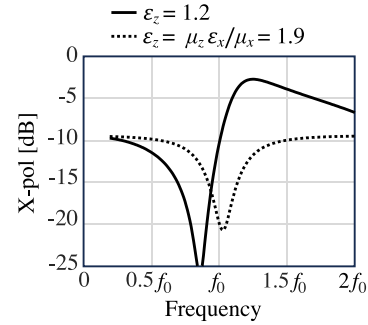


Fig. 10. X-pol for anisotropic slab above a grounded magnetic Wheeler current sheet, for different values of  $\epsilon_z$ .

example, the difference in refractive index for the TE and TM modes causes the ADL to exhibit higher X-pol as compared with an isotropic dielectric slab.

As an example, let us consider the ADL structure shown in Fig. 9(a), with  $p_{\text{ADL}} = 0.15\lambda_0$ ,  $w_1 = w_2 = 0.03\lambda_0$ ,  $w_3 = 0.007\lambda_0$ ,  $h_1 = 0.033\lambda_0$ ,  $h_2 = 0.013\lambda_0$ ,  $h_3 = 0.043\lambda_0$ , and  $h_4 = 0.013\lambda_0$ . The lower two ADLs are separated by a dielectric slab with relative permittivity  $\epsilon_r = 2.94$ . The ADL can be homogenized to retrieve the following equivalent relative permittivity and permeability tensors:

$$\begin{bmatrix} \epsilon_x & 0 & 0 \\ 0 & \epsilon_y & 0 \\ 0 & 0 & \epsilon_z \end{bmatrix} = \begin{bmatrix} 9.4 & 0 & 0 \\ 0 & 9.4 & 0 \\ 0 & 0 & 1.2 \end{bmatrix} \quad (24)$$

$$\begin{bmatrix} \mu_x & 0 & 0 \\ 0 & \mu_y & 0 \\ 0 & 0 & \mu_z \end{bmatrix} = \begin{bmatrix} 1 & 0 & 0 \\ 0 & 1 & 0 \\ 0 & 0 & 0.2 \end{bmatrix}. \quad (25)$$

As evident from (19), the  $z$ -component of the permittivity tensor  $\epsilon_z$  only affects the refractive index for the TM mode. If one imposes the condition  $n_{\text{TE}} = n_{\text{TM}}$ , and assumes that the ADLs consist of square patches (i.e.,  $\epsilon_x = \epsilon_y$  and  $\mu_x = \mu_y$ ), we obtain

$$\epsilon_z = \mu_z \epsilon_x / \mu_x. \quad (26)$$

To illustrate the effect of this condition, Fig. 10 shows the comparison of the X-pol of the homogenized slab with the values in (24) and (25) to the ones obtained by applying (26). Without the condition, the X-pol increases to approximately  $-2$  dB near  $f_0$ . With the condition in (26), which gives  $n_{\text{TE}} = n_{\text{TM}}$ , the X-pol is reduced to below the free-space value, similar to an isotropic slab.

### IV. SUPERSTRATES WITH REDUCED X-POL

One possible method to alter the  $z$ -component of the permittivity tensor is by including vertical metallic insertions such as vias, as shown in Fig. 11(a). These vias interact

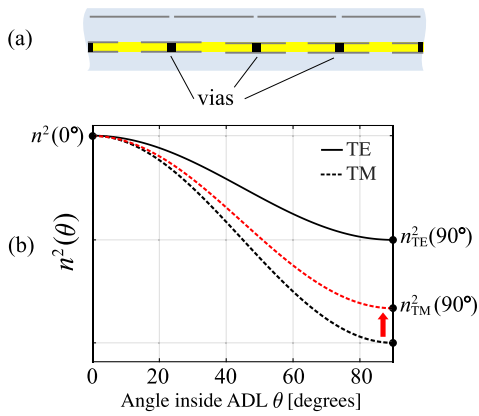


Fig. 11. Effect of increased  $\varepsilon_z$  on the equivalent TM refractive index of an ADL. (a) ADL structure with added vias connecting the patches in the lower two layers and (b) effect of increased  $\varepsilon_z$  on the equivalent TM refractive index.

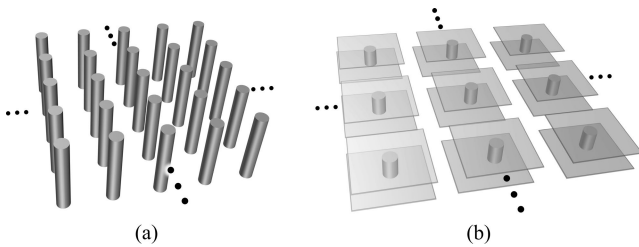


Fig. 12. (a) Wire medium and (b) combination of wire medium and square-patch ADLs, resulting in a capacitively loaded wire medium.

with the electric field along  $z$  and thereby increase  $\varepsilon_z$ . This reduces the difference between the TE and TM equivalent refractive indexes of the ADLs, as depicted in Fig. 11(b). Since an excessive increase of  $\varepsilon_z$  would cause surface waves in a realistic array, we include vias only between the two lowest layers of the ADL.

#### A. Wire Medium

Such vertical metal pins can be placed in a periodic square lattice along  $x$  and  $y$  to form a wire medium. This structure is illustrated in Fig. 12(a). The  $z$ -component of the permittivity can be tuned by adjusting the spacing between the pins or their length. If the wire medium is inserted as a separate slab between the metal layers of the ADL, the maximum length of the pins is limited. As such, to sufficiently increase the value of the  $z$ -component of the permittivity would require a very large number of closely spaced pins.

Fortunately, the effect of each pin on  $\varepsilon_z$  can be enhanced by connecting the vertical pins to the patches in the ADL. This adds capacitive loading to the pins and makes them behave as if they are effectively longer, so fewer pins can be used to achieve the same enhancement of  $\varepsilon_z$ . This combination of ADL and the wire medium is illustrated in Fig. 12(b), where vias are added to implement the vertical metal pins.

#### B. Application to Wideband Arrays

To give a realistic example of how the ADL is used in wideband array design, we consider the unit cell in Fig. 13(a), which shows a cavity-backed connected slot element, loaded with a four-layer ADL.

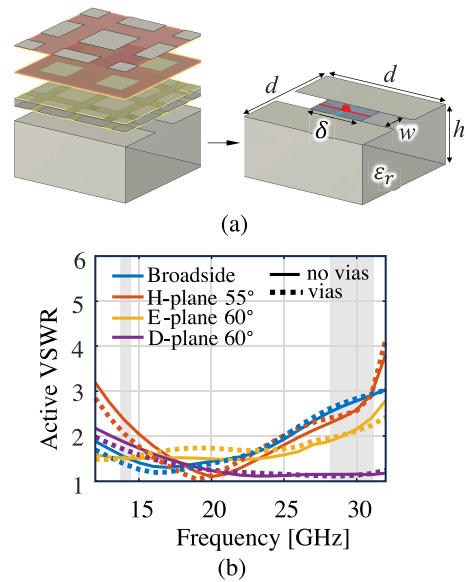


Fig. 13. (a) Three-dimensional view of the connected array unit cell with ADL superstrate and (b) simulated active VSWR.

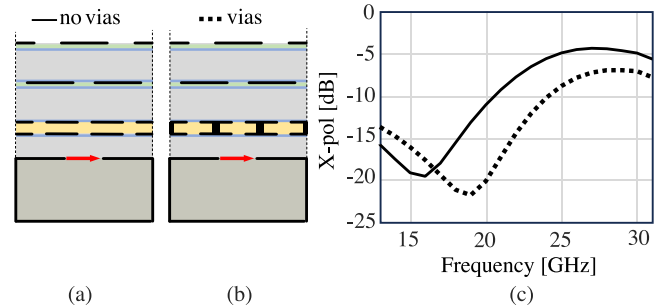


Fig. 14. Side view of the connected slot unit cell with an artificial dielectric (a) without and (b) with vertical vias. (c) Simulated X-pol.

The unit cell with periodicity  $d = 4.35$  mm consists of a connected slot with width  $w = 1$  mm, a delta-gap feed of length  $\delta = 1.87$  mm, placed at a distance  $h = 1.91$  mm from a backing reflector. The substrate between the backing reflector and the slot plane has a relative permittivity of  $\varepsilon_r = 1.7$  and contains vertical walls along the direction of the slots.

The design example covers simultaneously the Ku- and the Ka-transmit SatCom bands, 13.75–14.5 GHz (for Ku-band) and 28 to 31 GHz (for Ka-band) [17]. In Fig. 13(b), the unit cell's active voltage standing wave ratio (VSWR) is reported. The VSWR of the unit cell is lower than 3 for scanning up to  $55^\circ$  in the H-plane, and up to  $60^\circ$  in the D- and E-planes, for the two bands of interest (highlighted in gray).

The X-pol of this unit cell is calculated when scanning to  $60^\circ$  in the diagonal plane ( $\phi = 45^\circ$ ) for the stratification without vias [side view in Fig. 14(a)] and with vias [Fig. 14(b)]. The X-pol of the unit cell without vias in Fig. 14(c) exceeds  $-5$  dB for the upper frequencies. The X-pol of the unit cell with vias is shown to be significantly lowered due to the presence of the vias. As shown by the dotted lines in Fig. 13(b), the VSWR is not adversely affected by the inclusion of the vias.

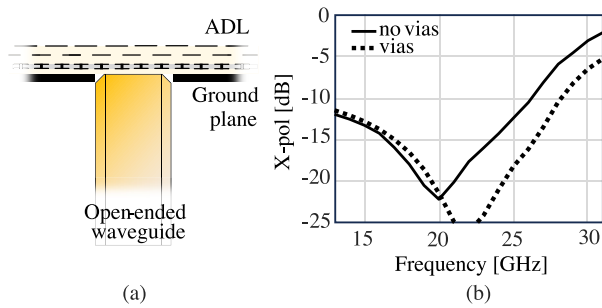


Fig. 15. (a) Open-ended waveguide loaded with the ADL structure and (b) simulated X-pol with and without vias.



Fig. 16. Photograph of the assembled prototype showing the top layer of the four-layer ADL over a ground plane in a mount that holds the WR28 waveguide.

## V. EXPERIMENTAL VALIDATION

### A. Measurement Setup

To independently assess the X-pol properties of the two ADLs, they are illuminated by a WR28 open-ended waveguide. A ground plane is placed under the ADL board, in which a hole is present through which the waveguide probe is inserted, as shown in Fig. 15(a). Although the behavior of the X-pol with respect to frequency is different compared with the array case, the improvement in terms of X-pol reduction achieved with the vias is similar in the two cases, as shown by the simulated X-pol in Fig. 15(b).

Two ADL boards were manufactured to experimentally verify the result: one with vias and one without. The details of the geometry and the used materials are listed in Appendix C. A photograph of the assembled sample, including the ADL board, a ground plane, and the waveguide probe, is shown in Fig. 16. Since the X-pol levels in the Ku-band are comparable between the two boards, the measurements are only performed for the Ka-band. A far-field measurement over a 26–36-GHz bandwidth is performed.

### B. Results

The measured co- and cross-components of the electric field are shown for the diagonal plane at 34 GHz in Fig. 17(a). It can be observed that a lower X-pol level is obtained in the case of vias. The X-pol ratio for both versions of the ADL is shown for the diagonal plane in Fig. 17(b), along with the change in X-pol between the boards. To show the

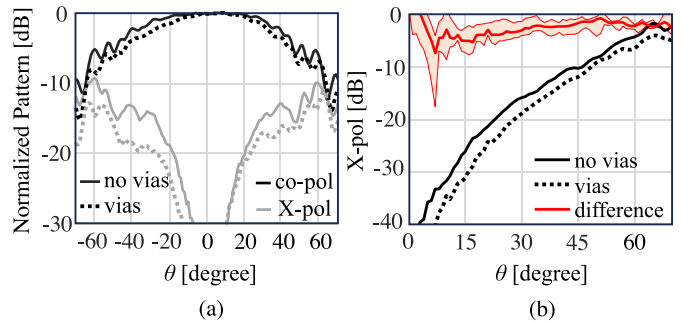


Fig. 17. (a) Measured normalized patterns at 34 GHz of the prototype in the diagonal plane ( $\phi = 45^\circ$ ) and (b) X-pol ratio and the change in X-pol on the diagonal plane between the ADL without and the ADL with wire medium.

improvement both in frequency and in scanning angle, the figure shows the average X-pol ratio in the 26–36-GHz band over a range of  $0^\circ$ – $70^\circ$ . The red line shows the mean change in X-pol over that frequency band and the shaded region shows the range of values found in the averaged band. It is seen that the mean change ranges from  $-5$  to  $-2$  dB. Despite some discrepancy between the simulated and measured values, the X-pol is consistently reduced by the presence of the vias over the entire band and scanning range. It can be noted that the X-pol change becomes positive at angles close to broadside, but this corresponds to very low levels of X-pol for both boards ( $< -35$  dB).

The reduction of 2–5 dB may not be sufficient for some applications, but the improvement shown here was mainly limited by the required bandwidth and scan range. In this example, we wanted to show that some X-pol reduction is possible while maintaining the scan range of  $\pm 60^\circ$  and the bandwidth 13.75–31 GHz. More significant reduction of X-pol is possible by placing more vias in each unit cell, at the expense of a reduced bandwidth or scan range.

## VI. CONCLUSION

A method for improving X-pol in wideband arrays that employ artificial dielectrics in their superstrate was presented. It was shown that the difference in the behavior of artificial dielectrics for TE and TM, which is desired for its positive effect on the scan volume and bandwidth, is also responsible for increased X-pol. A solution that employs vertical vias in the lower layers of the artificial dielectric has been shown to reduce the difference between the effective refractive index for the TE and TM modes. Simulations were presented to show this structure's effectiveness, and measurements showed a reduction in X-pol of 2–5 dB for up to  $70^\circ$  on the diagonal plane over a frequency range of 26–36 GHz.

## APPENDIX A

### FIELD RADIATED BY A WHEELER'S CURRENT

We consider an ideal  $x$ -oriented magnetic Wheeler's current sheet on a PEC plane with amplitude  $V_0$

$$m_x(x, y, z) = V_0 e^{-jk_x x} e^{-jk_y y} \delta(z) \quad (27)$$

where  $k_{x0} = k_0 \sin \theta \cos \phi$  and  $k_{y0} = k_0 \sin \theta \sin \phi$  are the  $x$ - and  $y$ -components of the propagation vector, and  $\delta$  represents a Dirac distribution. The quantity in (27) is a magnetic volume current density, with unit  $\text{V/m}^2$ . The Wheeler current radiates in the presence of a generic superstrate made of dielectrics or metal layers. The field radiated by such a current can be defined as follows:

$$\mathbf{e}_{\text{scat}}(\mathbf{r}) = \iiint \bar{\mathbf{g}}^{em}(\mathbf{r} - \mathbf{r}') m_x(\mathbf{r}') \hat{\mathbf{x}} d\mathbf{r}' \quad (28)$$

where  $\bar{\mathbf{g}}^{em}$  is the dyadic Green's function of the medium. Because the current is infinitesimally thin in  $z$ , from the volume current density  $m_x(x, y, z)$ , with units  $\text{V/m}^2$ , we can consider a surface magnetic current density  $m_{s,x}(x, y)$ , with units  $\text{V/m}$ . Hence, the radiation integral becomes

$$\mathbf{e}_{\text{scat}}(\mathbf{r}) = \int_{-\infty}^{\infty} \int_{-\infty}^{\infty} \bar{\mathbf{g}}^{em}(x - x', y - y', z) m_{s,x}(\mathbf{r}') \hat{\mathbf{x}} dx' dy' \quad (29)$$

where

$$m_{s,x}(x, y) = V_0 e^{-jk_{x0}x} e^{-jk_{y0}y}. \quad (30)$$

We can now write Green's function  $\bar{\mathbf{g}}^{em}$  as the inverse Fourier transform of the 2-D spectral Green's function  $\bar{\mathbf{G}}^{em}$

$$\begin{aligned} \bar{\mathbf{g}}^{em}(x - x', y - y', z) \\ = \frac{1}{4\pi^2} \int_{-\infty}^{\infty} \int_{-\infty}^{\infty} \bar{\mathbf{G}}^{em}(k_x, k_y, z) e^{-jk_x(x-x')} e^{-jk_y(y-y')} dx' dy'. \end{aligned} \quad (31)$$

The components of the dyadic spectral Green's function for an  $x$ -oriented magnetic current can be expressed in terms of the current and voltage solutions ( $i_{\text{TE}}$ ,  $i_{\text{TM}}$ ,  $v_{\text{TE}}$ , and  $v_{\text{TM}}$ ) of the equivalent transmission lines representing the stratification [see Fig. 1(b)]

$$\begin{bmatrix} G_{xx}^{em}(k_x, k_y, z) \\ G_{yx}^{em}(k_x, k_y, z) \\ G_{zx}^{em}(k_x, k_y, z) \end{bmatrix} = \begin{bmatrix} (v_{\text{TM}} - v_{\text{TE}})k_x k_y \\ k_\rho^2 \\ v_{\text{TE}}k_x^2 + v_{\text{TM}}k_y^2 \\ k_\rho^2 \\ -\frac{\zeta k_y}{k} i_{\text{TM}} \end{bmatrix} \quad (32)$$

where  $\zeta$  is the medium impedance at  $z$ . A step-by-step derivation of the spectral Green's function for stratified media can be found in [12].

Substituting (31) in the radiation integral (29) and recognizing that the Fourier transform of a constant distribution with a linear phase term is a Dirac  $\delta$ , i.e.,

$$\begin{aligned} \int_{-\infty}^{\infty} \int_{-\infty}^{\infty} e^{-jk_{x0}x'} e^{-jk_{y0}y'} e^{jk_x x'} e^{jk_y y'} dx' dy' \\ = 4\pi^2 \delta(k_x - k_{x0}) \delta(k_y - k_{y0}) \end{aligned} \quad (33)$$

the scattered field becomes

$$\begin{aligned} \mathbf{e}_{\text{scat}}(\mathbf{r}) = V_0 \int_{-\infty}^{\infty} \int_{-\infty}^{\infty} \bar{\mathbf{G}}^{em}(k_x, k_y, z) \hat{\mathbf{x}} \\ \cdot \delta(k_x - k_{x0}) \delta(k_y - k_{y0}) e^{-jk_x x} e^{-jk_y y} dk_x dk_y. \end{aligned} \quad (34)$$

From the property of the Dirac  $\delta$ , we can then close the integral as follows:

$$\mathbf{e}_{\text{scat}}(\mathbf{r}) = V_0 \bar{\mathbf{G}}^{em}(k_{x0}, k_{y0}, z) \hat{\mathbf{x}} e^{-jk_{x0}x} e^{-jk_{y0}y}. \quad (35)$$

Assuming that Green's function is calculated on the top of the dielectric stratification (at  $z = z_0$ ) and there is free space above, we can write

$$\begin{aligned} \mathbf{e}_{\text{scat}}(x, y, z_0) \\ = V_0 \bar{\mathbf{G}}^{em}(k_{x0}, k_{y0}, z_0) \hat{\mathbf{x}} e^{-jk_{x0}x} e^{-jk_{y0}y} e^{-jk_{z0}(z-z_0)} \end{aligned} \quad (36)$$

with  $k_{z0} = k_0 \cos \theta$  or in a more compact form

$$\mathbf{e}_{\text{scat}}(x, y, z_0) = V_0 \bar{\mathbf{G}}^{em}(k_{x0}, k_{y0}, z_0) \hat{\mathbf{x}} e^{-jk_0 r} \quad (37)$$

where  $r = \sqrt{x^2 + y^2 + (z - z_0)^2}$ . When calculating the X-pol levels of the Wheeler current, the term  $\exp(-jk_0 r)$  can be omitted without loss of generality since it multiplies both the co-polar and cross-polar components, and thus, it cancels out in the expression of the X-pol ratio.

## APPENDIX B

### LUDWIG THREE COMPONENTS OF THE RADIATION FROM WHEELER'S CURRENT

From (32) and (37), the Cartesian components of the radiated field from an  $x$ -oriented magnetic Wheeler current can be written explicitly as follows:

$$\begin{aligned} e_x &= V_0 (v_{\text{TM}} - v_{\text{TE}}) \sin \phi \cos \phi \\ e_y &= V_0 (v_{\text{TE}} \cos^2 \phi + v_{\text{TM}} \sin^2 \phi) \\ e_z &= -V_0 \zeta_0 i_{\text{TM}} \sin \theta \sin \phi. \end{aligned} \quad (38)$$

One can relate the Cartesian components of the field vector to the spherical components as follows:

$$\begin{aligned} e_\theta &= \cos \theta \cos \phi e_x + \cos \theta \sin \phi e_y - \sin \theta e_z \\ e_\phi &= -\sin \phi e_x + \cos \phi e_y. \end{aligned} \quad (39)$$

Since the fields are evaluated in free space, we can write the current  $i_{\text{TM}}$  in terms of the voltage  $v_{\text{TM}}$  as follows:

$$i_{\text{TM}} = \frac{v_{\text{TM}}}{Z_{\text{TM}}} = \frac{v_{\text{TM}}}{\frac{\zeta_0 k_z}{k_0}} = \frac{v_{\text{TM}}}{\frac{\zeta_0 k_0 \cos \theta}{k_0}} = \frac{v_{\text{TM}}}{\zeta_0 \cos \theta}. \quad (40)$$

By substituting (38) and (40) into (39) and using some algebraic steps, one finds the simple expressions

$$\begin{aligned} e_\theta &= V_0 v_{\text{TM}} \sin \phi \sec \theta \\ e_\phi &= V_0 v_{\text{TE}} \cos \phi. \end{aligned} \quad (41)$$

From the spherical components, one can find the projection on the co- and cross-polarization vectors, defined according to the third definition of Ludwig [13]

$$\begin{aligned} e_{\text{co}} &= V_0 (v_{\text{TM}} \sin^2 \phi \sec \theta + v_{\text{TE}} \cos^2 \phi) \\ e_{\text{cr}} &= V_0 \frac{\sin(2\phi)}{2} (v_{\text{TM}} \sec \theta - v_{\text{TE}}). \end{aligned} \quad (42)$$

TABLE I  
ADL DIMENSIONS [mm]

	$p$	$h$	$w$	$s$
Layer 1	1.45	0.5	0.36	0
Layer 2	1.45	0.254	0.36	0
Layer 3	2.175	0.8	1.1	0
Layer 4	2.175	0.8	0.75	1.09

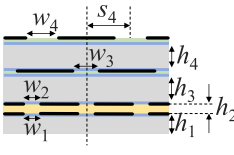


TABLE II  
ADL MATERIALS

	$\epsilon_r$	Thickness
 DuPont™ Pyralux® AP	3.4	25 $\mu\text{m}$
 Rogers CuClad® 6250	2.32	38 $\mu\text{m}$
 Rogers RT/duroid® 5880	2.2	254 $\mu\text{m}$
 Rohacell 31 HF®	1.04	Varies

### APPENDIX C GEOMETRICAL PARAMETERS OF THE ADL

The artificial dielectric is designed following the procedure described in [17] and consists of four layers which are defined by the unit cell periodicity  $p$ , their distance from the previous layer  $h$ , gap width  $w$ , and shift with respect to the previous layer  $s$ . The values for each layer are listed in Table I, starting at the bottom layer. Between layers 1 and 2, a dielectric with relative permittivity  $\epsilon_r = 2.2$  is present. In the ADL with vias, the patches in layers 1 and 2 are connected by a via with a diameter of 0.2 mm.

The materials used in the construction of the ADL are listed in Table II, where the colors match those illustrated in Table I. The thickness of the Rohacell 31 HF is not listed, as it varies to ensure the metal layers are separated by the distances listed in Table I.

### REFERENCES

- [1] J. T. Logan, R. W. Kindt, M. Y. Lee, and M. N. Vouvakis, "A new class of planar ultrawideband modular antenna arrays with improved bandwidth," *IEEE Trans. Antennas Propag.*, vol. 66, no. 2, pp. 692–701, Feb. 2018.
- [2] E. Yetisir, N. Ghalichechian, and J. L. Volakis, "Ultrawideband array with 70° scanning using FSS superstrate," *IEEE Trans. Antennas Propag.*, vol. 64, no. 10, pp. 4256–4265, Oct. 2016.
- [3] E. Magill and H. Wheeler, "Wide-angle impedance matching of a planar array antenna by a dielectric sheet," *IEEE Trans. Antennas Propag.*, vol. AP-14, no. 1, pp. 49–53, Jan. 1966.
- [4] S. Sajuyigbe, M. Ross, P. Geren, S. A. Cummer, M. H. Tanielian, and D. R. Smith, "Wide angle impedance matching metamaterials for waveguide-fed phased-array antennas," *IET Microw., Antennas Propag.*, vol. 4, no. 8, p. 1063, 2010.
- [5] T. R. Cameron and G. V. Eleftheriades, "Analysis and characterization of a wide-angle impedance matching metasurface for dipole phased arrays," *IEEE Trans. Antennas Propag.*, vol. 63, no. 9, pp. 3928–3938, Sep. 2015.
- [6] T. G. Waterman, "Wideband wide scan antenna matching structure using electrically floating plates," U.S. Patent 8 253 641 B1, Aug. 28, 2012.
- [7] W. H. Syed, D. Cavallo, H. T. Shivamurthy, and A. Neto, "Wideband, wide-scan planar array of connected slots loaded with artificial dielectric superstrates," *IEEE Trans. Antennas Propag.*, vol. 64, no. 2, pp. 543–553, Feb. 2016.

- [8] D. Cavallo, W. H. Syed, and A. Neto, "Connected-slot array with artificial dielectrics: A 6 to 15 GHz dual-pol wide-scan prototype," *IEEE Trans. Antennas Propag.*, vol. 66, no. 6, pp. 3201–3206, Jun. 2018.
- [9] A. Hoorfar, K. C. Gupta, and D. C. Chang, "Cross-polarization level in radiation from a microstrip dipole antenna," *IEEE Trans. Antennas Propag.*, vol. 36, no. 9, pp. 1197–1203, Sep. 1988.
- [10] C.-C. Chen, "Wideband wide-angle impedance matching and polarization characteristics of circular waveguide phased arrays," *IEEE Trans. Antennas Propag.*, vol. AP-22, no. 3, pp. 414–418, May 1974.
- [11] H. A. Wheeler, "Simple relations derived from a phased-array antenna made of an infinite current sheet," *IEEE Trans. Antennas Propag.*, vol. AP-13, no. 4, pp. 506–514, Jul. 1965.
- [12] D. Cavallo, "Connected array antennas: Analysis and design," Ph.D. Dissertation, Dept. Elect. Eng., Eindhoven Univ. Tech., Eindhoven, The Netherlands, 2011, pp. 147–166, doi: 10.6100/IR719461.
- [13] A. Ludwig, "The definition of cross polarization," *IEEE Trans. Antennas Propag.*, vol. AP-21, no. 1, pp. 116–119, Jan. 1973.
- [14] D. Cohen and R. Shavit, "Bi-anisotropic metamaterials effective constitutive parameters extraction using oblique incidence S-parameters method," *IEEE Trans. Antennas Propag.*, vol. 63, no. 5, pp. 2071–2078, May 2015.
- [15] D. Cavallo, W. H. Syed, and A. Neto, "Closed-form analysis of artificial dielectric layers—Part I: Properties of a single layer under plane-wave incidence," *IEEE Trans. Antennas Propag.*, vol. 62, no. 12, pp. 6256–6264, Dec. 2014.
- [16] R. M. van Schelven, D. Cavallo, and A. Neto, "Equivalent circuit models of finite slot antennas," *IEEE Trans. Antennas Propag.*, vol. 67, no. 7, pp. 4367–4376, Jul. 2019.
- [17] A. J. van Katwijk, A. Neto, G. Toso, and D. Cavallo, "Design of wideband wide-scanning dual-polarized phased array covering simultaneously both the Ku- and the Ka-satcom bands," in *Proc. 14th Eur. Conf. Antennas Propag. (EuCAP)*, Copenhagen, Denmark, Mar. 2020, pp. 1–3.



**Alexander J. van Katwijk** (Member, IEEE) received the B.Sc. and M.Sc. (cum laude) degrees in electrical engineering from Delft University of Technology (TU Delft), Delft, The Netherlands, in 2017 and 2019, respectively, where he is currently pursuing the Ph.D. degree with the Terahertz Sensing Group, with a focus on analytical/numerical techniques in electromagnetics, cross-polarization reduction techniques, and wideband connected arrays.



**Caspar M. Coco Martin** (Graduate Student Member, IEEE) received the M.Sc. degree (cum laude) in electrical engineering from Delft University of Technology (TU Delft), Delft, The Netherlands, in 2022, where he is currently pursuing the Ph.D. degree with the Terahertz Sensing Group.

His current research interests include wideband antenna arrays, artificial dielectrics, and analytical methods for electromagnetics.

Mr. Coco Martin was a recipient of the Excellent Presentation Award at the IEEE Ukrainian Microwave Week in 2022 and the Best Antenna Theory Paper Award at the 18th European Conference on Antennas and Propagation (EuCAP) in 2024.



**Giovanni Toso** (Fellow, IEEE) received the Laurea (cum laude) and Ph.D. degrees from the University of Florence, Florence, Italy, in 1992 and 1995, respectively.

During his Ph.D. and post-doctoral fellowship, he spent more than one year as a Visiting Scientist at the Laboratoire d'Optique Electromagnetique de Marseille, Marseille, France. In 1999, he was a Visiting Scientist with the University of California (UCLA) at Los Angeles, Los Angeles, CA, USA. In 2000, he was appointed as a Researcher at the

Radio Astronomy Observatory of the Italian National Council of Research (CNR), Rome, Italy. Since 2000, he has been with the Antenna and Sub-millimeter Waves Section, European Space Agency (ESA), European Space Research and Technology Centre (ESTEC), Noordwijk, The Netherlands. He has been initiating several research and development activities on satellite antennas based on arrays, reflectarrays, discrete lenses, and reflectors. In particular, in the field of onboard satellite antennas, he has been coordinating activities on multibeam antennas mainly for telecom applications. In the field of terminal antennas, he has been supporting the development of reconfigurable antennas with electronic, mechanical, and hybrid scanning; some of these antennas are now available as commercial products. He has promoted the development of the commercial software tool QUPES by TICRA, now used worldwide, for the analysis and design of periodic and quasi-periodic surfaces, such as reflectarrays, frequency selective surfaces, transmit arrays, and polarizers.

Dr. Toso received the Post-Doctoral Fellowship from the University of Florence in 1999; a Scholarship from Alenia Spazio, Rome, in 2000; and together with Prof. A. Skrivervik, the European School of Antennas (ESoA) Best Teacher Award in 2018. In 2014, he has been a Guest Editor, together with Dr. R. Mailloux, of the Special Issue on "Innovative Phased Array Antennas Based on Non-Regular Lattices and Overlapped Subarrays" published in IEEE TRANSACTIONS ON ANTENNAS AND PROPAGATION and, for the same society, was an Associate Editor, from 2013 to 2016. In 2018, he was the Chairperson of the 39th ESA Antenna Workshop on "Multibeam and Reconfigurable Antennas." Since 2010, together with Dr. P. Angeletti, he has been instructing short courses on multibeam antennas and beamforming networks during international conferences, such as the IEEE Antennas and Propagation Society (APS), IEEE-MTT International Microwave Symposium (IMS), IEEE International Conference on Wireless Technology and Systems (ICWITS), European Conference on Antennas and Propagation (EuCAP), and European Microwave Week (EuMW), which have been attended by more than 1100 participants. Together with Dr. P. Angeletti, he is the Organizer of the EurAAP-ESoA Course on Active Antennas. Together with Dr. E. Gandini, he is also the Organizer of the EurAAP-ESoA Course on satellite antennas,

one of the most consolidated ESoA Courses, attended so far by about 300 participants. He also received recognition at European Space Agency (ESA) for the outstanding contribution to the Artes Technology Workplan preparation 2024 in support of ESA research and development activities for Telecom Applications in November 2023. Since January 2023, has been elevated to IEEE Fellow grade for contributions to multibeam antenna developments for satellite applications. He is a Distinguished Lecturer of the IEEE Antennas and Propagation Society.



**Daniele Cavallo** (Senior Member, IEEE) received the M.Sc. degree (summa cum laude) in telecommunication engineering from the University of Sannio, Benevento, Italy, in 2007, and the Ph.D. degree (cum laude) in electromagnetics from Eindhoven University of Technology, Eindhoven, The Netherlands, in 2011.

From 2007 to 2011, he was with the Antenna Group, Netherlands Organization for Applied Scientific Research, The Hague, The Netherlands.

From 2012 to 2015, he was a Post-Doctoral

Researcher with the Microelectronics Department, Delft University of Technology (TU Delft), Delft, The Netherlands. In 2015, he joined the Chalmers University of Technology, Gothenburg, Sweden, as a Visiting Researcher. He is currently an Associate Professor with the Terahertz Sensing Group, TU Delft. He has authored or coauthored about 200 papers published in peer-reviewed international journals and conference proceedings. His current research interests include wideband antenna arrays, analytical and numerical methods for antenna characterization, and millimeter-wave integrated antennas.

Dr. Cavallo was a recipient of the Best Innovative Paper Prize at the European Space Agency Antenna Workshop in 2008, the Best Paper Award in Electromagnetics and Antenna Theory at the 11th European Conference on Antennas and Propagation (EuCAP) in 2017, the Best Antenna Theory Paper at EuCAP 2024, and the 250 keuro "Veni" Personal Grant from the Netherlands Organization for Scientific Research in 2015. His students received the Best Student Paper Award at EuCAP 2013, the Special Mention at EuCAP 2015, the Else Kooi Prize in 2016, and the Honorable Mention at the IEEE Antennas and Propagation Society International Symposium in 2019. He is the Co-Coordinator of the EurAAP working group "Active Array Antennas," and a Management Committee Member of the COST Action "Future communications with higher-symmetric engineered artificial materials (SyMat)." He has served as an Associate Editor for IEEE TRANSACTIONS ON ANTENNAS AND PROPAGATION from 2016 to 2023.